ISPRS Journal of Photogrammetry and Remote Sensing 141 (2018) 176–184

Contents lists available at ScienceDirect

ISPRS Journal of Photogrammetry and Remote Sensing

journal homepage: www.elsevier.com/locate/isprsjprs

Detection flying aircraft from Landsat 8 OLI data

F. Zhao[a,b,1], L. Xia[b,c,1], A. Kylling[d], R.Q. Li[a], H. Shang[b], Ming Xu[a,b,*]

[a] *Key Laboratory of Ecosystem Network Observation and Modeling, Institute of Geographic Sciences and Natural Resources Research, University of Chinese Academy of Science, Beijing, China*
[b] *Department of Ecology, Evolution and Natural Resources, Rutgers University, New Brunswick, NJ 08901, USA*
[c] *Beijing Research Center of Intelligent Equipment for Agriculture, Beijing Academy of Agriculture and Forestry Sciences, Beijing, China*
[d] *NILU-Norwegian Institute for Air Research, Kjeller, Norway*

ARTICLE INFO

Keywords:
Landsat 8
1.38 µm
Aircraft detection

ABSTRACT

Monitoring flying aircraft from satellite data is important for evaluating the climate impact caused by the global aviation industry. However, due to the small size of aircraft and the complex surface types, it is almost impossible to identify aircraft from satellite data with moderate resolution, e.g. 30 m. In this study, the 1.38 µm water vapor absorption channel, often used for cirrus cloud or ash detection, is for the first time used to monitor flying aircraft from Landsat 8 data. The basic theory behind the detection of flying aircraft is that in the 1.38 µm channel most of the background reflectance between the ground and the aircraft is masked due to the strong water vapor absorption, while the signal of the flying aircraft will be attenuated less due to the low water vapor content between the satellite and the aircraft. A new composition of the Laplacian and Sobel operators for segmenting aircraft and other features were used to identify the flying aircraft. The Landsat 8 Operational Land Imager (OLI) 2.1 µm channel was used to make the method succeed under low vapor content. The accuracy assessment based on 65 Landsat 8 images indicated that the percentage of leakage is 3.18% and the percentage of false alarm is 0.532%.

1. Introduction

The growing aviation fleet raises concerns about how to monitor the aircraft activity and evaluate the climate impact of the aviation industry (Burkhardt and Kärcher, 2011). According to the report from the Intergovernmental Panel on Climate Change (IPCC), aviation produces around 2% of the world's manmade emissions of carbon dioxide (CO_2), an important but inconclusive global radiative forcing caused by the contrail cirrus, and small amounts of soot particles, nitrogen oxides etc. (Penner, 1999). Contrail cirrus with line-shape formed initially by the cruising aircraft is one of the important anthropogenic contributions to the global radiative forcing (Sausen et al., 2005). While automated contrail tracking algorithms exist (Vazquez-Navarro et al, 2010), it is generally difficult to track contrail cirrus and distinguish the contrail cirrus from natural cirrus in satellite remote sensing data directly. Thus, current research aiming to understand the radiative forcing caused by the contrail cirrus is mainly based on model simulation, which faces many uncertainties, such as, many simplifying assumptions used in the model, lack of observation data of contrail cirrus and optical depth, and no enough observation radiance data to validate and improve the simulation model (Minnis et al., 1999; Ponater et al., 2002; Schumann 2012; Chen and Gettelman, 2013; Bock and Burkhardt, 2016).

Currently, the most efficient ways to track the activity of aircraft are ground radar and Automatic Dependent Surveillance Broadcast (ADS-B) receiver. Both the radar and ADS-B receiver are ground devices, and each of them provides coverage ranges from tens to hundreds of kilometers. The main problem of these ground devices is that uncovered area cannot provide any information about the aircraft. Besides, aircraft detection based on satellite remote sensing image with high spatial resolution is also being presented, and several studies have been made to recognize aircrafts from such images (Zhang and Zhou, 2007; Wu et al., 2015). These approaches mainly adopted some digital image processing and classification algorithms which depend on the high resolution of the images for aircraft detection, e.g. corner detection, neural network, and wavelet transform (Benedetto et al., 2012). But high spatial resolution satellite images are not suitable to monitor the aircraft activity globally, because high spatial resolution satellite images are heavily influenced by clouds and have a long revisit cycle.

The moderate-resolution Earth observation satellites, such as Landsat 7/8 and Sentinel 2, have spatial resolution around 10–60 m and a short revisit cycle (16-day for Landsat 8 and 5-day for Sentinel 2 A B) to image the entire Earth (Roy et al., 2014; Shoko and Mutanga, 2017). Compared

---

[*] Corresponding author at: Department of Ecology, Evolution and Natural Resources, Rutgers University, New Brunswick, NJ 08901, USA.
E-mail address: mingxu@igsnrr.ac.cn (M. Xu).

[1] Contributed equally to this work.

https://doi.org/10.1016/j.isprsjprs.2018.05.001
Received 14 September 2017; Received in revised form 1 May 2018; Accepted 1 May 2018

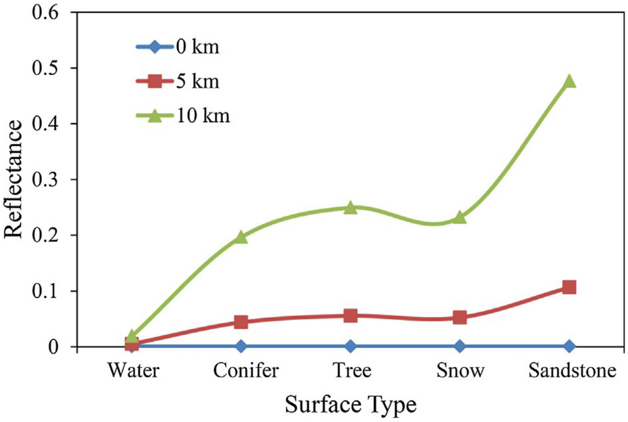

Fig. 1. Simulated reflectances for five types of background surfaces at altitudes of 0 km, 5 km, 10 km. Spectral information of these materials was obtained from the NASA Jet Propulsion Laboratory (JPL) spectral library (Baldridge et al., 2009).

with high resolution satellites, the spatial resolutions of these moderate-resolution Earth observation satellites are the primary limitation factor when using the above methods to recognize aircraft. Hence, there is no research in the literature about how to identify aircraft from these data so far. The 1.38 μm water vapor absorption channels of Landsat 8 and Sentinel 2 with 30 m and 60 m resolutions respectively, provide an opportunity to monitor flying aircraft. In this study, we presented a technique to detect flying aircraft using these channels, and this method is for the first time to give us an opportunity to observe the global aviation activity. The detection results will be useful for tracing the aircraft activity and subsequently evaluating the impacts of radiative forcing and pollution caused by the global aviation industry.

2. Algorithm

2.1. Basic theory

Sitting on the edge of a very strong line of water vapor absorption, the 1.38 μm channel is usually used to monitor cirrus cloud, furthermore, it is sensitive to scattering objects (Xia et al., 2015). When the water vapor content is sufficiently high, the 1.38 μm signal from the surface is masked by the absorption of water vapor, but objects at high altitudes, e.g. high cloud, cirrus cloud or volcanic ash are less influenced for the reason that water vapor content between them and the satellite is relatively low. Hence, the 1.38 μm channel is often used to monitor cirrus cloud and track volcanic ash (Gao et al., 1993; Gao and Kaufman, 1995; Frey et al., 2008; Xia et al., 2018).

The top of atmosphere (TOA) reflectance of the OLI band 9 was simulated by the libRadtran radiative transfer software package version 2.0.1 for five kinds of surface types at different altitudes above sea level (Mayer and Kylling, 2005; Emde et al., 2016), as shown in Fig. 1. The mid-latitude standard model atmosphere was used and the vapor content was set to 2.0 g/cm^2. As can be seen from the figure, as the altitude of the surface increases, the reflectance increases, the surfaces at low altitude present a small reflectance compared with the surfaces at higher altitudes. This also implies that an aircraft at a high altitude will present a larger signal than the background. Thus, under the condition of enough water vapor content, most of the background noise will be masked out in the 1.38 μm channel, and the aircraft signal is enhanced, which is just what is needed. Fig. 2(a) and (d) provide an example. Fig. 2(a) is a true color composite image (red, green and blue bands) and (b) is the OLI 1.38 μm band. The white point in the center of Fig. 2(d) is a cruising aircraft. It is obvious that the aircraft is difficult to be automatically detected in Fig. 2(a), a true color image with complex background information. In fact, for a cloudy scene, or over bright surface types e.g. snow, city, etc., it is extremely difficult to identify the aircraft even by manual inspection. However, due to the strong absorption of water vapor in the 1.38 μm band, the background signals are greatly attenuated, while the signal of the cruising aircraft at high altitude is less influenced. Therefore, it is easy to identify an aircraft using this channel. As shown in Fig. 2(b), a cruising aircraft with contrail cirrus behind can be readily identified.

Fig. 2(a) and (d) demonstrate an ideal situation that no cloud is in the sky and the vapor content is large enough to mask the ground information. In general, scenes covered by cloud or with a dry atmosphere in winter are more common, as shown in Fig. 2 (b), (e) and (c), (f) respectively. Fig. 2(b) is an image obtained in a dry atmosphere, and the 1.38 μm channel failed to mask the ground information, which is

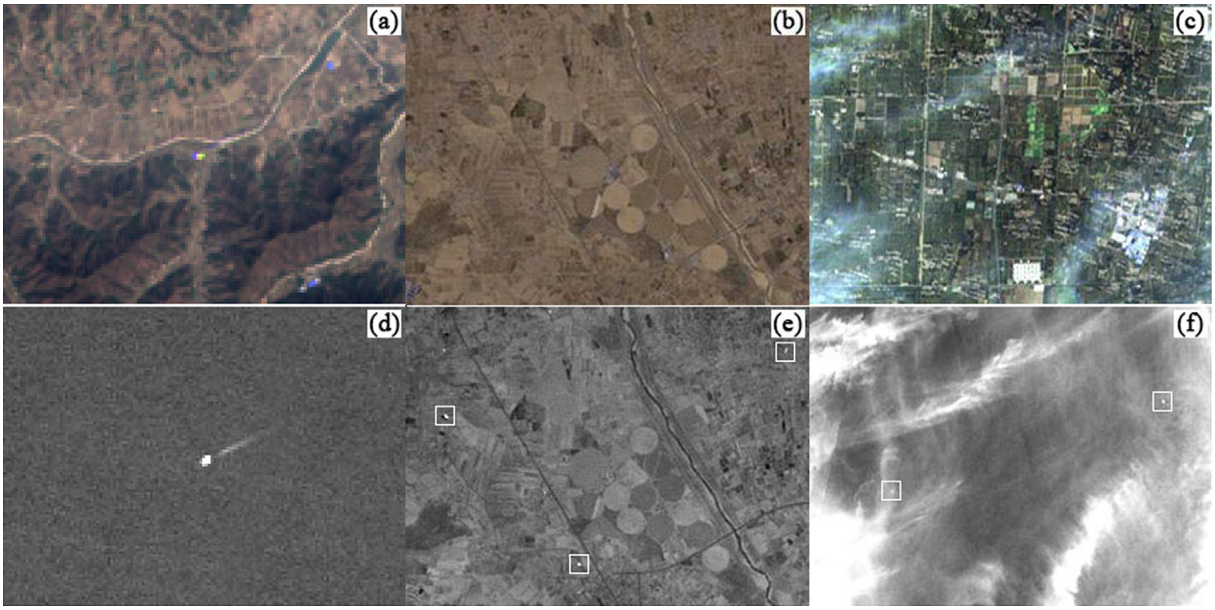

Fig. 2. (a), (b) and (c) are Landsat 8 OLI true color images, (d), (e) and (f) are images of the OLI band 9. Data of (a), (b), (c) were obtained on 13 February 2015, Path 121/Row 38; 1 April 2017, Path 127/Row 32; and 30 April 2017, Path 121/Row 036, respectively. (For interpretation of the references to colour in this figure legend, the reader is referred to the web version of this article.)

presented in Fig. 2(e). In practice, there is no aircraft in the scene of Fig. 2(b), but Fig. 2(e) indicates the existence of aircrafts. For example, white points shown in the white rectangles of Fig. 2(e) look like aircraft, but they are indeed the objects of land with high reflectance in 1.38 μm channel. Fig. 2 c) is an image obtained in cloudy and moist conditions, Fig. 2(f) is the corresponding image of the 1.38 μm channel. The white pixel surrounded by the white rectangle on the right is an aircraft, while the other one in the left white rectangle is not an aircraft. Obviously, the left one leads to a great difficulty to identify the aircraft correctly. Thus, in order to detect aircrafts for general scenes accurately, the algorithm should work not only for ideal situations, but also for cloudy and dry atmospheric conditions.

2.2. Cloudy scene

As shown in Fig. 2, the shape of an aircraft presented in the image is similar to a point. According to the theory of point detection in digital image processing, an effective operator to detect isolated points is the Laplacian operator (Al-Amri et al., 2010). The Laplacian operator is a second order differential operator, which is described in Eq. (1).

$$\nabla^2(f(x, y)) = \frac{\partial^2 f(x, y)}{\partial x^2} + \frac{\partial^2 f(x, y)}{\partial y^2} \tag{1}$$

Here $f(x, y)$ is the Digital Number (DN) value of the image at row and column of x, y. $\frac{\partial^2 f(x,y)}{\partial x^2}$ and $\frac{\partial^2 f(x,y)}{\partial y^2}$ are second partial derivatives along the x and y spatial axes respectively. Rather than using the Laplacian directly, this study conducted image segmentation first, and then some morphological rules were adopted to identify aircraft. Image segmentation was carried on using the new combination of the Sobel and Laplacian operator (we call it SL), as shown in Eq. (2).

$$g(x, y) = \nabla^2((f_{sobel}(x, y)) \tag{2}$$

Eq. (2) means that the Sobel operator $f_{sobel}(x, y)$ (Gonzalez et al., 2008) is used to process the image of the OLI band 9 first, then the Laplacian $\nabla^2(f_{sobel}(x, y))$ is used to segment the result of the Sobel operator, and $g(x, y)$ is the final segmentation result. After differentiating Eq. (1) with respect to x, y, Eq. (2) can be written as

$$g(x, y) = \nabla^2(f_{sobel}(x, y)) = f_{sobel}(x+1, y) + f_{sobel}(x-1, y) + f_{sobel}(x, y+1) + f_{sobel}(x, y-1) - 4f_{sobel}(x, y) \tag{3}$$

Usually, first-order derivatives generally produce thicker edges in an image, and second-order derivatives produce a stronger response to fine detail, e.g. thin line, isolated point. Second-order derivatives are stronger in enhancing sharp changes so that it cannot be used to obtain the full edge of the objects in the OLI image directly, such as, cloud, aircraft etc. But by using the Sobel operator to produce the thicker edge first (Gonzalez et al., 2008), the second-order derivative does not

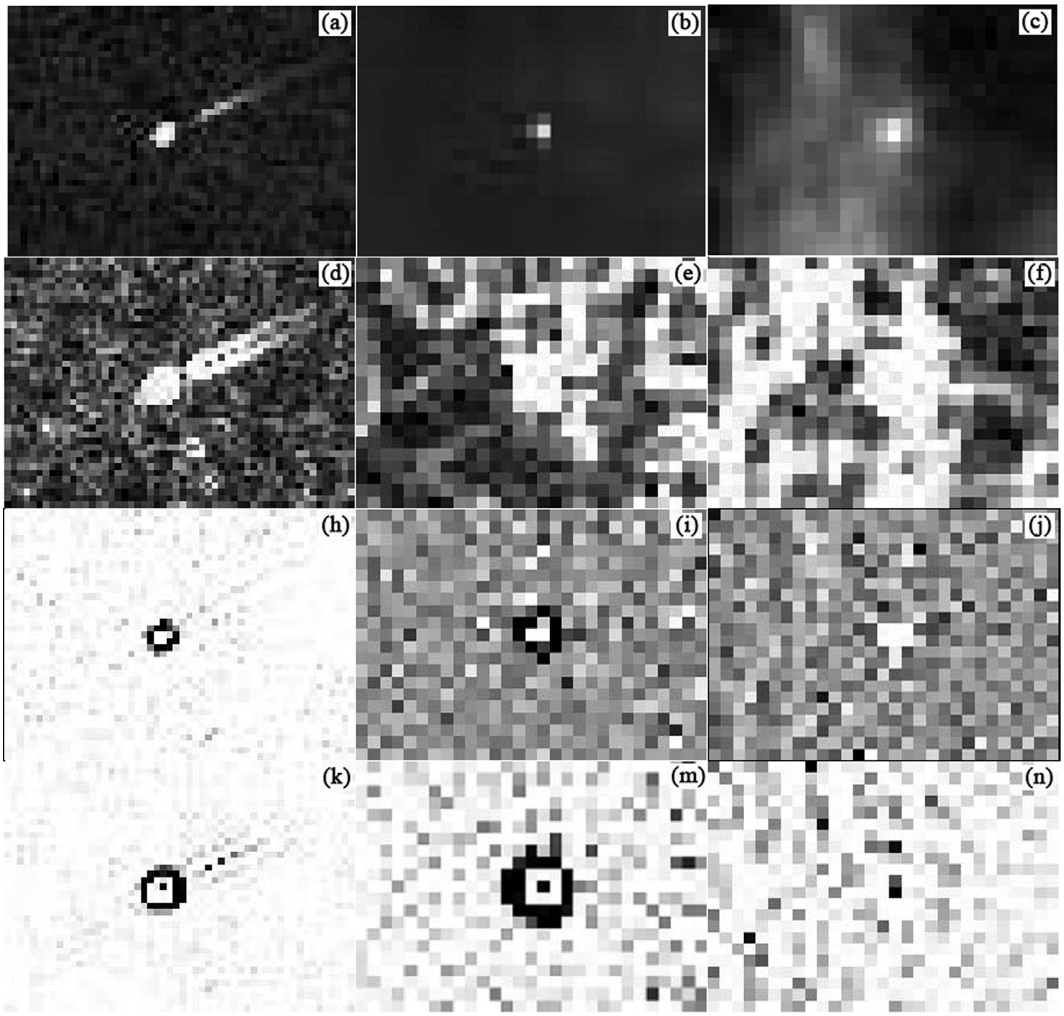

Fig. 3. (a), (b) and (c) are images of the OLI band 9; (d), (e) and (f) are images of Sobel filter for (a), (b) and (c); (h), (i) and (j) are images of Laplacian filter for (a), (b) and (c); (k), (m) and (n) are images of SL filter for (a), (b) and (c).

perform as strong as when used alone, and the full edge of the aircraft is obtained reasonably. Besides, the reason why the Sobel filter (2-dimensional mask) is adopted instead of the first-order derivative operator (1-dimensional mask) is that the Sobel operator is symmetric about the center point and produces a thicker edge than the first-order derivative operator. Fig. 3 illustrates these points.

Fig. 3(a) and (b) are magnifications of the image part including aircrafts as shown in Fig. 2(d) and (f), Fig. 3 (c) is the magnified image of the white rectangle on the left of Fig. 2(f). As can be seen in Fig. 3(d), (e), and (f), Sobel filter produces thicker edges for not only the aircrafts, but also clouds. The Laplacian results presented in Fig. 3(h), (i) and (j) indicate the stronger response in enhancing sharp change, hence the narrower edges are obtained. The images in Fig. 3(h) and (i) demonstrate that the Laplacian may detect aircrafts well. Specifically, after using the Laplacian to filter the image of the OLI band 9, if the points with DN value greater than 500 is surrounded by a closed edge with negative points (four neighborhoods), then the points will be recognized as aircraft. This detection rule is called RULE1. However, Fig. 3(j) indicates that RULE1 may cause false alarm under a cloudy scene, as the point of the aircraft in Fig. 3(j) presented similar feature with RULE1. On the other hand, Fig. 3(a) and (k), (b) and (m) indicate that the SL detects the edge of the aircraft well. The point of cloud which was falsely segmented by the Laplacian, as shown in Fig. 3(j), is not falsely segmented by the SL, and there is no notable edge observed in Fig. 3(n). Besides, the SL provides the maximum DN value of the aircraft in the image of the 1.38 μm channel, as the dark points shown in the center of Fig. 3(k) and (m). The dark point is called the maximum value point (*MVP*), and the maximum DN value of aircraft in the image of the 1.38 μm channel is called the maximum value point of aircraft (*MVPA*). In this study, the rule used to segment the potential aircraft from the image was that the value of *MVP* was less than −500, and the *MVP* was surrounded by a dark edge with DN value less than −100.

After obtaining the segmented image of potential aircraft, we used a rule to determine whether the segmentation result can be identified as an aircraft, as shown in Eq. (4).

$$Aircraft = \begin{cases} true,\ R_{asp} > 0.45\ \ and\ \ R_{pix} > 0.6\ \ and\ \ 6 < N_{airc} < 15 \\ \qquad and\ \ DN_{MVPA} > Max(S) \\ \qquad false,\ otherwise \end{cases} \tag{4}$$

where $R_{asp}$is the aspect ratio of the segmented image, N_{airc} indicates the pixel number of potential aircraft in the segmented image (the white pixels with DN value great than 0 were surrounded by the dark edge, as shown in Fig. 3(k) and (m)), R_{pix}indicates the ratio of $N_{airc}$and the total pixel number of the segmented image (the points of the dark broad are not included), $DN_{MVPA}$is the DN value of *MVPA*, *S*is a square with a width of 15 pixels and at the center of *MVPA*, $Max(S)$is the maximum pixel value of the *S*. *Aircraft*is the aircraft detection result.

Besides, in summer, the isolated ice clouds in some images of the OLI band 9 in South America are similar to aircraft. In this case, false alarms would be produced when using Eq. (4). To overcome this problem, the feature of cloud shadow was used to eliminate the false alarms in this study. An isolated ice cloud and a fast-moving aircraft present similar reflectance, but the slow-moving cloud will cause more prominent shadow than the fast-moving aircraft. Hence, in the summer of South America, when the DN value of *MVPA*'s four neighbor is less than the mean DN value of the *S*, the object will be identified as cloud.

2.3. Dry atmospheric condition

Vapor content is the main factor influencing the background signal of the 1.38 μm channel. When the vapor content is not large enough to mask the background signal, the background can be seen clearly in the OLI 1.38 μm channel, as shown in Fig. 4(a). Fig. 4 is the Landsat 8 image obtained on April 1, 2017, Path 127/Row 032, geolocation of 109.636/40.647, and the total column precipitable water vapor is about 0.33 g/cm^2 for this area (data source: MODIS MOD05 L2 vapor content data (Kaufman and Gao, 1992)). As can be seen in Fig. 4(a), due to the low vapor content, the OLI 1.38 μm channel fails to mask the background information so that the surface objects can be observed easily. As a result, false alarms labeled by the white rectangles in

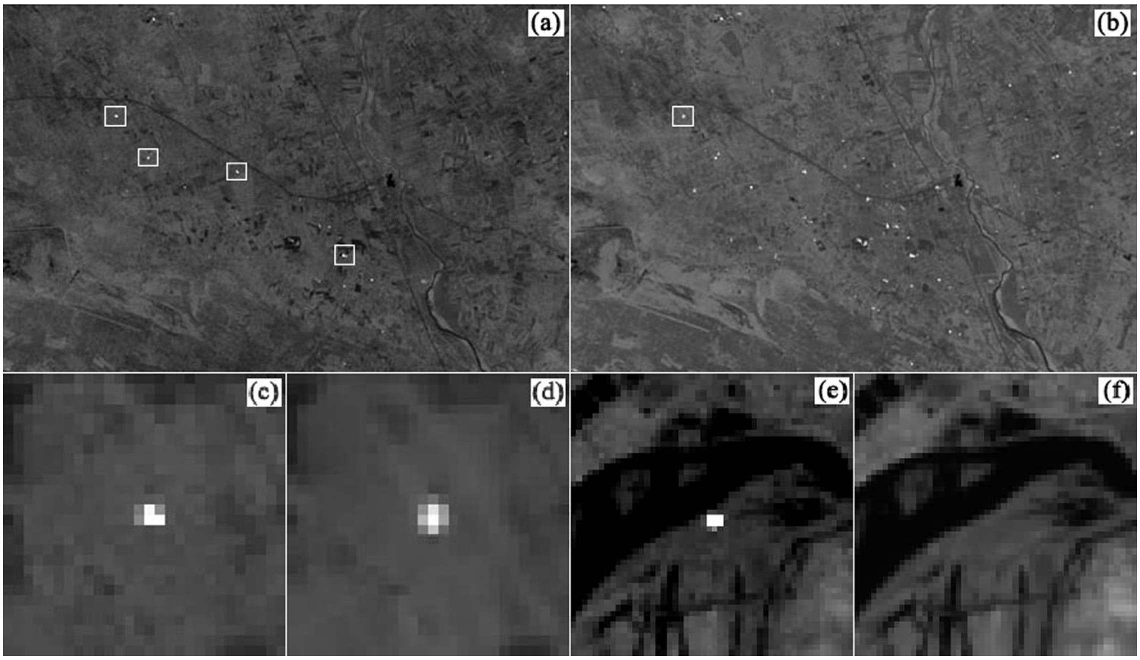

Fig. 4. (a) is an image of the OLI band 9 under low vapor content. The white rectangles shown in (a) are the positions of false alarm when Eq. (4) was used to conduct the detection; (b) is an image of the OLI 2.1 μm channel; (c) is the enlarged diagram of the leftmost white rectangle in Fig. 4 (a); (d) is the enlarged diagram of the white rectangle in Fig. 4(b); (e) presents an image of the OLI band 9 with an aircraft under low vapor content; (f) presents an image of the OLI 2.1 μm channel with the same location as (e).

Fig. 4(a), were caused by those high reflectance pixels when using the method presented in Eq. (4). In practice, the water vapor content is not always sufficiently large to mask the background signal in some regions with high altitude, or in the winter. Hence, in order to make the 1.38 μm channel applicable over these regions with extremely low vapor content, an extension of the current method is proposed.

To make the algorithm perform well in a dry atmosphere condition, the OLI 2.1 μm channel and the push broom characteristic of OLI were used. As an atmospheric window band, 2.1 μm is less attenuated by aerosol, thin cirrus etc. Hence, it is often used to retrieve aerosol optical thickness (Levy et al., 2007) and remove thin cirrus contamination of a solar spectral band between approximately 0.4 and 1.0 μm (Richter et al., 2011; Gao and Li, 2012). Fig. 4(a) and (b) show images of the same geographical position in the OLI 1.38 μm and the 2.1 μm channels respectively. As can be seen in Fig. 4(a) and (b), pixels with large reflectance in the 1.38 μm channel show large reflectance in the 2.1 μm channel too, and pixels with small reflectance in both Fig. 4(a) and (b) present similar reflectance. Besides, according to the JPL spectral library (Baldridge et al., 2009), pixels of object with high reflectance, such as man-made buildings, standalone etc. in 1.38 μm have similar reflectance in 2.1 μm.

The focal plane array of OLI consists of fourteen individual focal plane modules aligned in a staggered line (Knight and Kvaran, 2014). Each focal plane module includes nine rows of detectors for the OLI nine channels, which are stacked in this order: panchromatic, blue, coastal/aerosol, NIR, red, green, SWIR2, SWIR1, and cirrus in track direction (Irons et al., 2012). The stack order of the nine channels and the push broom feature of OLI cause the slight offset for each band image if no additional correction was performed. For example, for the data of Landsat 8 collection 1 that had been registered to the ground, a stationary object has the same numbers of column and row in each band. But for a fast motion object, e.g. a flying aircraft, due to no correction for it, the object may have different numbers of column and row in each band. This indicates that for a pixel with large reflectance in the image of the OLI 1.38 μm channel, if the pixel represents the surface object, the pixel with the same column and row in the image of the OLI 2.1 μm channel will give large reflectance too. Fig. 4(c) and (d) present this feature. Fig. 4(c) is the enlargement of the leftmost white rectangle of the OLI 1.38 channel in Fig. 4(a), and (d) is the enlargement of the OLI 2.1 channel of the white rectangle at the same location in Fig. 4(b). As it can be seen from Fig. 4(c) and (d), the number of row and column for the maximum DN value of Fig. 4(c) and (d) are the same. But this feature is not true for a flying aircraft in the images of the 1.38 μm channel and the 2.1 μm channel, as shown in Fig. 4(e) and (f). Fig. 4(e) is the image of the OLI band 9 with an aircraft under vapor content of 0.33 g/cm^2, Fig. 4(f) is the image of the OLI 2.1 μm channel with the same location as Fig. 4(e). Due to the imaging characteristic shown above, an aircraft in the OLI band 9 could not be found at the same location of the OLI 2.1 μm channel.

Considering the features discussed above, this study utilized these features to make the algorithm work under low vapor condition. If pixels were identified as aircraft by Eq. (4) and vapor content was less than a threshold, Eq. (5) was used to eliminate false alarms.

$$Aircraft = \begin{cases} true, & DN_{i,j} < AccPer_{0.95}(Hist(S)) \\ false, & otherwise \end{cases} \tag{5}$$

Here i, j is the numbers of row and column of MVP. $DN_{i,j}$ is image DN value of the 2.1 μm channel with row and column of i, j. S is a square with a width of 15 pixels and at the center of i and j. $Hist(S)$ is the histogram result of S. $AccPer_{0.95}(Hist(S))$ is the DN value which accumulation percentage in the $Hist(S)$ is greater than 0.95. According to the simulation and practical observation of the OLI band 9 data, the

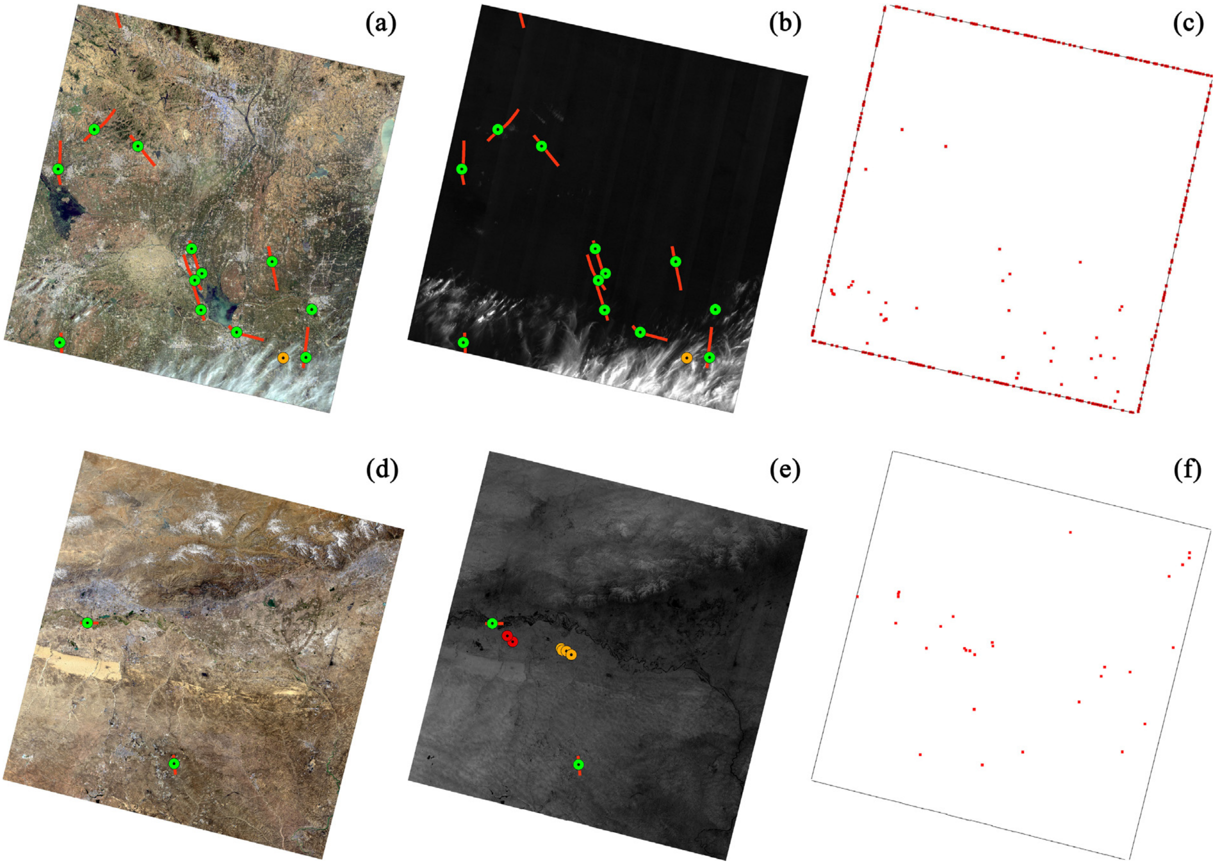

Fig. 5. (a) (d) are true color images; (b) (e) are the images of cirrus channel; (c) is the detection result by RULE1, (f) is the detection result by Eq. (4); red points in (c) and (f) are flying aircrafts. (For interpretation of the references to colour in this figure legend, the reader is referred to the web version of this article.)

threshold of vapor content is set to 0.8 g/cm^2. After using Eq. (5) to conduct the detection, the false alarms showed in Fig. 4(a) were totally removed, and the final test result can be seen in Fig. 5.

3. Validation and application

Validation is a necessary part for an algorithm to be used confidently. The detailed algorithm used in this study was presented in Section 2. In this section, validation of the accuracy of the algorithm is conducted.

3.1. Data and processing

Regions well covered by the ground aircraft tracker were selected as the validation regions in the study, and manual interpretation of Landsat 8 scenes and the real-time aircraft monitoring data from Flightradar24 were obtained as the true aircrafts information in the validation. The atmospheric water vapor content data used is from the European Centre for Medium-Range Weather Forecasts (ECMWF) reanalysis data ERA-Interim (Dee et al., 2011), of which, the daily water vapor content data was used.

The real-time aircraft monitoring data from Flightradar24 (https://www.flightradar24.com/) was adopted as independent verification of aircraft location. In consideration of the OLI band 9 with a resolution of 30 m, thus, aircrafts with length less than 30 m were removed from the real-time aircraft monitoring data. Besides, aircrafts with flight altitude less than 5 000 m were also removed from the real-time aircraft monitoring data. The manual interpretation was carefully done by combining the image features of the OLI 1.38 μm and 2.1 μm channels, and the real-time aircraft monitoring data was used as reference. For those aircrafts covered by the high cloud and thus could not be observed from the image of the OLI 1.38 μm channel, but could be found from the real-time aircraft monitoring data, the manual interpretation would exclude them.

Besides, except for the influence of high cloud, it should be noted that the real-time flight data did not cover all the aircrafts for some reasons. First, not all the aircrafts were equipped with automatic dependent surveillance-broadcast (ADS-B) or similar devices. Except this reason, some aircrafts were limited for security reasons. Thus, the result of manual interpretation may differ from the real-time flight data. In this study, due to the algorithm being based on the 1.38 μm channel image, the final accuracy assessment would use the result of manual interpretation as the validation data, and the real-time aircraft monitoring data was selected as a reference.

3.2. Results

Two examples of Landsat image are presented in Fig. 5, of which, one was obtained under enough vapor content, and another one was a scene in a very dry atmosphere. Landsat 8 image used in the test obtained on April 30, 2017 with geolocation of latitude 34.693, longitude 118.161, Path 121/Row 36 was one of the examples imaging in a condition of enough vapor content, as shown in Fig. 5(a), (b) and (c). Fig. 5(a) is the true color composite image (red, green and blue bands), Fig. 5(b) is the image of the cirrus channel, and Fig. 5(c) is the aircraft detection result only used by RULE1. From Fig. 5(a) and (b), it can be seen that this Landsat image is composed of city, cropland, forest, water and high cloud etc.

Real-time aircraft monitoring data in the time ranging from 02:41:00 to 02:43:00 were selected to compose the flight paths, as the red lines shown in Fig. 5(a) and (b). The imaging time of the center scene of this Landsat image was 02:42:17, thus the aircrafts identified in the study should be the same here along the flight paths created by the real-time aircraft monitoring data. The aircraft shown in Fig. 2(f) is located in the right-bottom corner, and the aircraft likely to be a cloud as shown in Fig. 2(f) is represented by the yellow points in Fig. 5(a) and (b).

Green circles shown in Fig. 5(a) and (b) are aircrafts identified by manual interpretation and obtained by Eq. (4) respectively. As can be seen from Fig. 5(a) and (b), the real-time aircraft monitoring data and the manual interpretation result show similar result, and just one aircraft difference exists between them. In fact, the real-time aircraft monitoring data lost one aircraft in the region of this OLI data. Compared with the manual interpretation result, the results shown in Fig. 5(a) indicate that Eq. (4) detects aircrafts reasonably well. The detection by RULE1, Fig. 5(c), caused a large number of false alarms for the region covered with high cloud, which is shown in the right-bottom region of Fig. 5(b). Besides, a large number of pixels near the edge of the image were also falsely identified as aircrafts. The reason for this problem was that the drastic gray change near the edge pixels presented similar feature as the aircraft shown in the image.

Landsat 8 OLI data obtained under low vapor content was partly used in Fig. 2(b) (e) and Fig. 4, and this data was also selected to conduct the test, as shown in Fig. 5(d), (e) and (f). The results of manual interpretation and detection algorithm are presented in Fig. 5(d) and (e), as the green circles indicated in figures. Red lines are the real-time flight paths of aircrafts. The aircraft likely points shown in Fig. 2(b), (e) and Fig. 4(a) are labeled in Fig. 5(e) with red and yellow circles. As can be seen from Fig. 5(e), none of these points are falsely recognized as aircrafts. Since these data were obtained under low vapor content, the background objects in the OLI band 9 could be observed clearly. When the OLI band 7 was not used to enhance the detection, that is to say the test was only conducted based on Eq. (4), a large number of false alarms occurred, as shown in Fig. 5(f). But when the OLI band 7 was used to conduct the detection, all the false alarms were eliminated and no additional leakage was caused, as the green circles and the real-time aircraft flight paths shown in Fig. 5(d) and (e).

Quantitative validation of the algorithm was done by using 65 Landsat 8 images obtained from June 1, 2017 to July 30, 2017 over different regions: China, America, Europe, Africa and Australia. These images include a variety of background surfaces, e.g., desert, urban, forest, grass, and mountains, different coverage of clouds and different water vapor content. Among these regions, the OLI images used in China are more covered by high cloud than other regions. The water vapor content in Australia is relatively low, but in America, Europe and China, the vapor contents are relatively ample. All the images were

Table 1
Results of accuracy validation for the algorithm.

Region	Path/Row	Image Num.	Aircraft Num.	Manual		Real-Time		Accuracy (%)	
				False	Leakage	False	Leakage	False	Leakage
America	27-28/33-34	14	153	1	3	3	8	0.65	1.96
Europe	197-198/26-27	12	229	2	6	5	22	0.87	2.62
China	123-124/38-39	14	79	0	6	3	54	0	7.59
Australia	93-94/84-85	12	27	0	1	2	2	0	3.70
Africa	171-172/47-48	13	78	0	2	2	2	0	2.56
Total		65	566	3	18	15	88	0.532	3.18

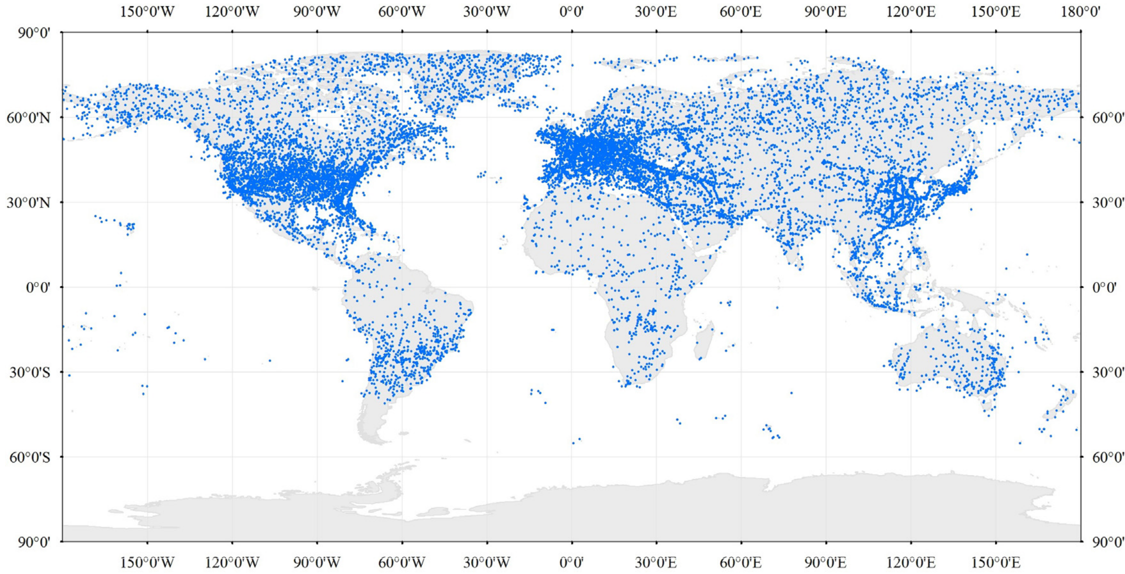

Fig. 6. Aircrafts detected between June 15 and 30, 2016 from Landsat OLI images.

manually interpreted, and the real-time aircraft monitoring data was used as the validation data, as shown in Table 1.

The detailed comparison data for the manual interpretation and real-time aircraft monitoring data was divided into two groups (false alarm and leakage) to evaluate the accuracy of algorithm better. The false alarm meant the algorithm in this study recognized other objects as aircrafts, the leakage indicated the algorithm failed to identify aircrafts. The columns of false and leakage in Table 1 show the false alarm and leakage for the algorithm respectively. The data summarized as 'Manual' column was created through manual interpretation of aircrafts from evaluated images, whereas 'Real-Time' represents the real-time aircraft monitoring data. Besides, as mentioned above, the mean accuracy of the algorithm was obtained by using the manual interpretation results as real data of the flying aircrafts, as the column of Accuracy shown in the table.

As shown in the table, the algorithm presents a large leakage when compared to the real-time aircraft monitoring data over a cloudy region, e.g. China. This was due to the reason that in a cloudy scene, the signal of the aircraft was often masked by high cloud so that the aircraft could not be found from the image of the 1.38 μm channel. On the other hand, the high cloud also increased the background reflectance, which made the reflectance difference between the aircraft and background not noticeable. The separation and recognition of the aircraft for a cloudy scene were more difficult than for a clear scene. Thus, leakage of manual interpretation in China was large, with the percentage of leakage 7.59%. But for other regions with less cloud coverage, e.g. Africa, Australia, America, the percentages of leakage were lower than it in China. False alarms of the real-time aircraft monitoring data indicated that the algorithm recognized 15 other objects as aircrafts in all the test data. However, the result of the manual interpretation showed that only 3 aircrafts were falsely recognized. This difference was due to that the real-time aircraft monitoring data failed to monitor the aircrafts caught by the OLI 1.38 μm channel, and the reason for this has been described in the beginning of Section 3.1.

Among the regions under the condition of a dry atmosphere, e.g. Australia, there are no notable false alarms produced. The percentages of leakage over these regions were lower compared to the percentage of leakage in the region of China, for the region of Australia the percentage of leakage was 3.7%. This indicates that using the OLI 2.1 μm channel to enhance the test would not decrease the leakage significantly. In general, the mean percentage of the leakage was 3.18% for the all test data, and the mean percentage of false alarm was 0.532%. This meant the algorithm presented in the study achieved a reasonable accuracy.

3.3. Application

Landsat 8 OLI images obtained from June 15, 2016 to June 30, 2016 (total number of these scenes is 11 430) were selected to produce the activity map of aircrafts globally. If the Sun elevation was less than 5 degree, the scene would be removed from the test. The monitoring result of aircrafts is shown in Fig. 6. In general, most of these scenes were obtained under a condition with enough vapor content, but the scenes over Greenland, Tibet, or Southern Africa, Australia and the Andes in the Southern America were obtained under a dry atmosphere. As can be seen, the algorithm performed well over the regions with a dry atmosphere, because there is no dense concentration of aircrafts over these regions.

As shown in Fig. 6, most of the aircrafts are distributed over the Northern Hemisphere, and in the Southern Hemisphere, aircrafts are mainly located over Southern Africa, and the center of South America. In the North Hemisphere, the most densely areas of aircrafts are America in the North America, Europe, and East Asia. As we can find from Fig. 6, the density of the aircraft is significantly related to economic development level of the region, the better its economy, the greater the number of aircrafts.

July is winter in the Antarctica and Landsat images in this region are unavailable, thus there is no aircraft found in this region. Aircrafts shown in the northern regions, e.g., Greenland, north of Russia, Canada, are fairly dense. The reason for this is that most of intercontinental flights prefer to pass through the Arctic to reduce the length of flights.

Table 2
Distribution of aircrafts for each continent.

Region	Aircraft number	Area (10 000 km^2)	Density (10 000 km^2)
Asia	3640	4457.9	0.82
Africa	586	3006.5	0.19
Europe	3142	993.8	3.16
Oceania	262	768.7	0.34
Antarctica	/	/	/
North America	5123	2425.6	2.11
South America	598	1781.9	0.34
Total Ocean	3936		
In all	17287		

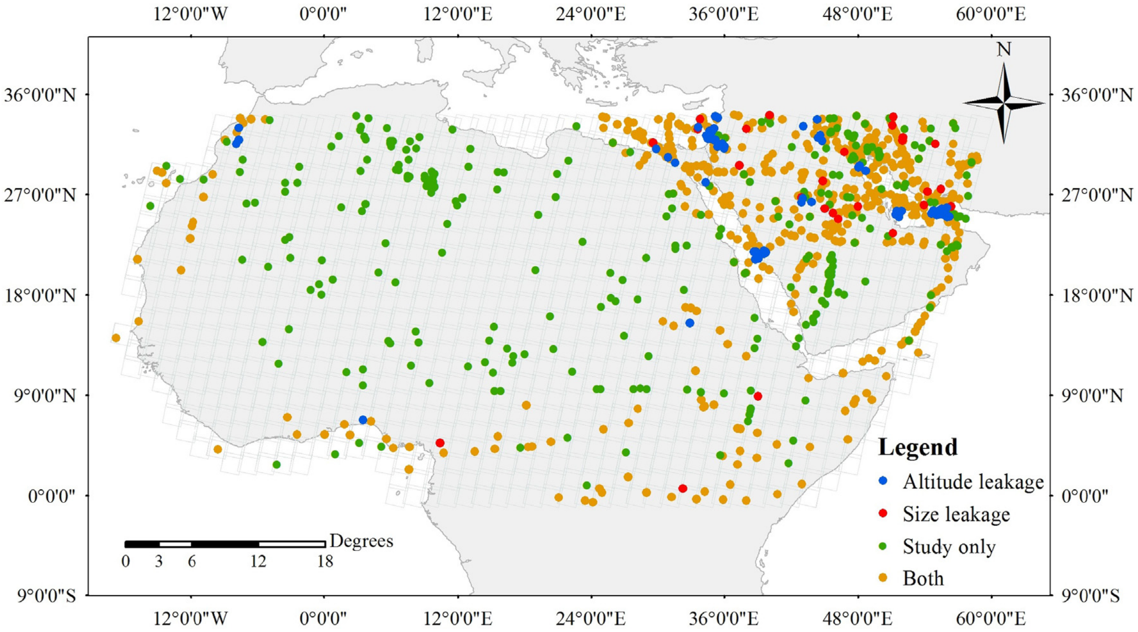

Fig. 7. Aircrafts detected by the real-time data and the study over northern Africa and West Asia, gray polygons are the border of Landsat images.

Besides, as a polar satellite, Landsat 8 has a shorter revisit time at polar regions than equator, thus, in an entire repeat cycle of 16-day, the polar regions are covered more than once.

The amount of the aviation-induced particles and gases emissions, such as, carbon dioxide (CO_2), water vapor, nitrogen oxides, black carbon etc., and contrail cirrus that caused radiative forcing are mainly determined by the number of the flying aircrafts. Hence, a simple statistic of distribution of aircrafts for each continent was made, the results are listed in Table 2. North America presents the largest number of aircraft compared to other continents, and Oceania has the smallest number of aircrafts among all the continents. Average aircraft density of each continent was calculated. As can be seen from Table 1, Europe has the densest flight activity with the value of 3.16 aircraft per 10 000 km^2, and Africa has the lowest flight activity with the value of 0.19 aircraft per 10 000 km^2. In all, a number of 17,287 aircrafts were detected from the 16-day of Landsat 8 images.

3.4. Discussion

The method of real-time aircraft monitoring based on the ground devices, e.g. radar, ADS-B receiver, is an effective way to provide the tracking information of aircraft. The method in this study relied on the Landsat 8 cirrus band presented a new way to monitor the global aircraft activity. These two methods are based on different theories, thus it is necessary to make a comparison about main differences between these two methods.

Firstly, these two methods have different temporal resolutions. The algorithm of this study used the Landsat 8 band 9 as the data source, and the Landsat 8 sensor can only obtain the image in a certain area when it passes. Therefore, this study can only capture the flying activity at the moment of satellite passing by, and the repeat cycle is as same as the Landsat 8 (16 days). But the real-time method can monitor the flight activity continuously as long as the ground devices perform well. Secondly, they differ in monitoring coverage. The real-time monitoring method requires enough and stable ground coverage for trace devices and stable internet access. In other words, it could not provide any information of the flight activity for regions with poor coverage for devices. The Landsat 8 has the ability of global observation, thus it is not limited to a specific area.

Finally, in consideration of security and privacy, some aircrafts observed by the ground devices are filter by the data provider. By contrast, the method in the study was not subject to such problem and could provide more comprehensive information of the flight activity. Of course, it still faces some challenges: (a) the data source used in the study is Landsat 8 band 9 with a resolution of 30 m, which means that aircraft with resolution around 30 m or less than 30 m may not be detected; (b) as described in Section 2, the lower the altitude, the weaker the signal of aircraft, hence, aircraft with low altitude will not be easily detected by this method; (c) if an aircraft flies below the high cloud with large optical depth, the signal of aircraft will be masked. As a result, it increases uncertainty for the algorithm to separate and recognize the aircraft. Also, if there exist the high cloud or other objects (e.g. volcano ash, balloons etc.) with shape like aircraft, the algorithm may identify them falsely.

The Landsat 8 images over northern Africa and West Asia from June 20, 2017 to July 6, 2017, and real-time flight data were selected to describe these main differences, as shown in Fig. 7. No matter the size and flight altitude, all the real-time flight data was selected, and this data was matched with the image of Landsat 8 band 9 in term of the imagining time and coverage. The matching results were divided into four parts: aircrafts identified by both of two methods (yellow points), aircrafts detected only by the method in this study (green points), aircrafts with size less than 30 m which traced by the ground devices only (red points, 12 aircrafts left out by this study also fell into this part), and aircrafts with flight altitude less than 5000 m which traced by the ground devices only (blue points).

As can be seen from Fig. 7, due to the lack of coverage for ground devices, the real-time flight data failed to monitor aircrafts around the Sahara, but the method presented in this study was not influenced by the coverage problem, as the green points shown in Fig. 7. For the region with nice coverage for ground devices, e.g. Middle East region, regions out of Sahara, as the yellow points shown in Fig. 7, the result from real-time data was reasonable. Besides, for aircrafts with small size less than 30 m or low altitude (5000 m), the study failed to detect them, as the blue and red points shown in Fig. 7[2] respectively. In practice, the aircraft mainly fly at the cruising height greater than 5000 m during the entire flight activity, and the stages of takeoff and

---

[2] For interpretation of color in Fig. 7, the reader is referred to the web version of this article.

landing are small parts of the whole flight. This means only few aircrafts will be lose by the study. In general, the method of this study was suitable to monitor cruising aircrafts with size no less than 30 m around the world.

4. Conclusions

The water vapor absorption channel near the center of 1.38 μm is not only useful for cirrus cloud detection, but also for detection of flying aircraft. The Landsat 8 OLI band 9 originally designed for cloud detection is highly effective for monitoring the activity of the flying aircraft. In this study, by using the combination of the Laplacian and Sobel operators, potential aircrafts were segmented from the Landsat 8 OLI band 9 images, and some features were used to identify the aircraft. The OLI band 7 and the push broom characteristic of OLI were used to make the algorithm work under a dry condition. Accuracy assessment based on 65 Landsat 8 images indicated that the algorithm achieved a reasonable accuracy, the percentage of leakage was 3.18% and the percentage of false alarm was 0.532%. The application of the method indicated that the global ability of monitoring aircraft from moderate resolution satellite data is for the first time established.

Acknowledgments

The authors would thank to USGS, NASA for providing Landsat 8 data and MODIS MOD05 data, ECMWF for providing vapor content data, and flight24 for providing the real-time flight data. We are grateful for support from the National Key R&D Program of China-Climate Change Impact and Adaptation in Major Countries along the Belt and Road (2018YFA0606500), National Key R&D Program of China (2017YFA0604302).

References

Al-Amri, S.S., Kalyankar, N.V., Khamitkar, S.D., 2010. Image segmentation by using edge detection. Int. J. Comp. Sci. Eng. 2 (3), 804–807.

Baldridge, A.M., Hook, S.J., Grove, C.I., Rivera, G., 2009. The ASTER spectral library version 2.0. Remote Sens. Environ. 113 (4), 711–715.

Benedetto, F., Fulginei, F.R., Laudani, A., Albanese, G. 2012. Automatic Aircraft Target Recognition by ISAR Image Processing Based on Neural Classifier.

Burkhardt, U., Kärcher, B., 2011. Global radiative forcing from contrail cirrus. Nat. Clim. Change 1 (1), 54–58.

Bock, L., Burkhardt, U., 2016. Reassessing properties and radiative forcing of contrail cirrus using a climate model. J. Geophys. Res.: Atmos. 121 (16), 9717–9736.

Chen, C.C., Gettelman, A., 2013. Simulated radiative forcing from contrails and contrail cirrus. Atmos. Chem. Phys. 13 (24), 12525–12536.

Dee, D.P., Uppala, S.M., Simmons, A.J., Berrisford, P., Poli, P., Kobayashi, S., Bechtold, P., 2011. The ERA-Interim reanalysis: configuration and performance of the data assimilation system. Quart. J. Royal Meteorological Soc. 137 (656), 553–597.

Emde, C., Buras-Schnell, R., Kylling, A., Mayer, B., Gasteiger, J., Hamann, U., ... Bugliaro, L., 2016. The libRadtran software package for radiative transfer calculations (version 2.0. 1). Geosci. Model Devel. 9 (5), 1647–1672.

Frey, R.A., Ackerman, S.A., Liu, Y., Strabala, K.I., Zhang, H., Key, J.R., Wang, X., 2008. Cloud detection with MODIS. Part I: improvements in the MODIS cloud mask for collection 5. J. Atmos. Oceanic Technol. 25 (7), 1057–1072.

Gonzalez, R.C., Woods, R.E., Eddins, S.L., 2008. Morphological image processing. Digital Image Process. 3, 627–688.

Gao, B.C., Li, R.R., 2012. Removal of thin cirrus scattering effects for remote sensing of ocean color from space. IEEE Geosci. Remote Sens. Lett. 9 (5), 972–976.

Gao, B.C., Kaufman, Y.J., 1995. Selection of the 1.375-μm MODIS channel for remote sensing of cirrus clouds and stratospheric aerosols from space. J. Atmos. Sci. 52 (23), 4231–4237.

Gao, B., Goetz, A.F., Wiscombe, W.J., 1993. Cirrus cloud detection from airborne imaging spectrometer data using the 1.38 μm water vapor band. Geophys. Res. Lett. 20 (4), 301–304.

Irons, J.R., Dwyer, J.L., Barsi, J.A., 2012. The next Landsat satellite: the Landsat data continuity mission. Remote Sens. Environ. 122, 11–21.

Knight, E.J., Kvaran, G., 2014. Landsat-8 operational land imager design, characterization and performance. Remote Sens. 6 (11), 10286–10305.

Kaufman, Y.J., Gao, B.C., 1992. Remote sensing of water vapor in the near IR from EOS/MODIS. IEEE Trans. Geosci. Remote Sens. 30 (5), 871–884.

Levy, R.C., Remer, L.A., Mattoo, S., Vermote, E.F., Kaufman, Y.J., 2007. Second-generation operational algorithm: retrieval of aerosol properties over land from inversion of moderate resolution imaging spectroradiometer spectral reflectance. J. Geophys. Res.: Atmos. 112 (D13).

Mayer, B., Kylling, A., 2005. Technical note: the libRadtran software package for radiative transfer calclations – description and examples of use. Atmos. Chem. Phys. 5, 1855–1877.

Minnis, P., Schumann, U., Doelling, D.R., Gierens, K.M., Fahey, D.W., 1999. Global distribution of contrail radiative forcing. Geophys. Res. Lett. 26 (13), 1853–1856.

Ponater, M., Marquart, S., Sausen, R., 2002. Contrails in a comprehensive global climate model: parameterization and radiative forcing results. J. Geophys. Res.: Atmos. 107 (D13).

Penner, J.E., 1999. Aviation and the Global Atmosphere: A Special Report of the Intergovernmental Panel on Climate Change. Cambridge University Press.

Roy, D.P., Wulder, M.A., Loveland, T.R., Woodcock, C.E., Allen, R.G., Anderson, M.C., et al., 2014. Landsat-8: science and product vision for terrestrial global change research. Remote Sens. Environ. 145 (145), 154–172.

Richter, R., Wang, X., Bachmann, M., Schläpfer, D., 2011. Correction of cirrus effects in Sentinel-2 type of imagery. Int. J. Remote Sens. 32 (10), 2931–2941.

Shoko, C., Mutanga, O., 2017. Examining the strength of the newly-launched Sentinel 2 MSI sensor in detecting and discriminating subtle differences between C3 and C4 grass species. ISPRS J. Photogramm. Remote Sens. 129, 32–40.

Sausen, R., Isaksen, I., Grewe, V., Hauglustaine, D., Lee, D.S., Myhre, G., Zerefos, C., 2005. Aviation radiative forcing in 2000: an update on IPCC (1999). Meteorologische Zeitschrift 14 (4), 555–561.

Schumann, U., 2012. A contrail cirrus prediction model. Geosci. Model Dev. 5, 543–580.

Vazquez-Navarro, M., Mannstein, H., Mayer, B., 2010. An automatic contrail tracking algorithm. Atmos. Meas. Tech. 3, 1089–1101.

Wu, Q., Sun, H., Sun, X., Zhang, D., Fu, K., Wang, H., 2015. Aircraft recognition in high-resolution optical satellite remote sensing images. IEEE Geosci. Remote Sens. Lett. 12 (1), 112–116.

Xia, L., Zhao, F., Ma, Y., Sun, Z.W., Shen, X.Y., Mao, K.B., 2015. An Improved algorithm for the detection of Cirrus clouds in the Tibetan Plateau using VIIRS and MODIS data. J. Atmos. Oceanic Technol. 32 (11), 2125–2129.

Xia, L., Zhao, F., Chen, L., Zhang, R., Mao, K., Kylling, A., Ma, Y., 2018. Performance comparison of the MODIS and the VIIRS 1.38 μm cirrus cloud channels using libRadtran and CALIOP data. Remote Sens. Environ. 206, 363–374.

Zhang, S.J., Zhou, Q., 2007. Aircraft type recognition in satellite images based on weighted-wavelet-fractal feature. Microelectron. Comp. 6, 051.